PCCP

Zinc blende versus wurtzite ZnS nanoparticles: Control of the phase and optical properties by tetrabutylammonium hydroxide

Journal:	*Physical Chemistry Chemical Physics*
Manuscript ID:	CP-ART-06-2014-002611.R1
Article Type:	Paper
Date Submitted by the Author:	28-Jul-2014

Complete List of Authors:	La Porta, Felipe; Universidade Estadual Paulista, Andres, Juan; Universitat Jaume I, Li, Máximo; Universidade de São Paulo-USP, Instituto de Física de São Carlos-IFSC Sambrano, Julio; Universidade Estadual Paulista, Dep. de Matematica Varela, Jose Arana; Universidade Estadual Paulista Julio de Mesquita Filho, Instituto de Quimica de Araraquara, Departamento de Fisico-Quimica Longo, Elson; Universidade Estadual Paulista, Instituto de Química

Journal Name

RSCPublishing

ARTICLE

Zinc blende *versus* wurtzite ZnS nanoparticles: Control of the phase and optical properties by tetrabutylammonium hydroxide

Cite this: DOI: 10.1039/xoxxoooooox

Received ooth January 2012,
Accepted ooth January 2012

DOI: 10.1039/xoxxoooooox

www.rsc.org/

F. A. La Porta,[*a, b] J. Andrés,[b] M. S. Li,[c] J. R. Sambrano,[d] J. A. Varela[a] and E. Longo[a]

The influence of tetrabutylammonium hydroxide on the phase composition (cubic zinc blende versus hexagonal wurtzite) of ZnS nanoparticles was studied. The ZnS nanoparticles were prepared by a microwave-assisted solvothermal method, and the phase structure and optical properties along with the growth process of ZnS nanoparticles were studied. We report XRD, FE-SEM, EDXS, UV-vis and PL measurements, and first-principle calculations based on TDDFT methods in order to investigate the structural and electronic properties and growth mechanism of ZnS nanostructures. The effects as well as the merits of microwave heating on the process and characteristics of the obtained ZnS nanostructure and their performance are reported.

1. Introduction

An increased interest in zinc sulfide (ZnS) nanomaterials has arisen mainly due to their application in different technological fields such as optoelectronic luminescent devices and photovoltaic cells [1-5]. The synthesis of ZnS nanocrystals with tunable size and phase not only provides alternative variables in tailoring the physical properties of this semiconductor material, but is also vital to develop them as building blocks in constructing the future nanoscale optoelectronic devices using the so-called "bottom-up" approach whereby atoms and molecules self-organize into nano-sized crystals or more complex molecular assemblies [6,7]. ZnS can adopt three phases: cubic zinc blende, hexagonal wurtzite or the rarely observed cubic rock salt [8]. Cubic zinc blende structure of ZnS is most stable form in the bulk which transforms into hexagonal wurtzite structure at 1020 °C, and melts at 1650 °C and both ZnS polymorphs have industrial applications [9,10]. In both cubic and hexagonal structures, Zn and S atoms are tetrahedrally bonded where the only difference is in the stacking sequence of atomic layers. Nevertheless, with decreasing particle size, the relative stability of two phases changes and low-temperature synthesis of small wurtzite ZnS nanoparticles have been reported [11-14], and very recently, Kulkarni et al. [15] reported the ethylenediamine-mediated wurtzite phase formation in ZnS. Controlled fabrication of nanoparticles with different phases is desirable and necessary, which however they are still a great challenges.

The kinetics of crystal growth strongly depend on the structure of the material, the properties of the solution, and the nature of the interface between the crystals and the surrounding solution [16-18]. In particular, the size dependence of the solid-solid phase transition temperature of ZnS nanoparticles has been the subject of intensive study [11,19,20], but harnessing the thermodynamic performance of the nanoparticles in a controllable way remains a complicated matter. Phase control in the growth of ZnS crystal is important, because each phase has unique physical properties, for instance, the different phases show different lattice vibration properties and nonlinear optical coefficients [21,22].

As the current research moves toward nanoscale phenomena and technology, the exploration of facile and economic methods for the synthesis of ZnS nanostructures of great interest. However, the crystal structure of the nanoparticle strongly depends on the synthesis conditions. Zhang et al. [23] by combining molecular dynamics simulations and experimental measurements suggests that wurtzite particles with size smaller than about 7 nm, *in vacuo*, are

more stable than zinc blende *in vacuo* at room temperature, however, lowering of the temperature of the zinc blende to wurtzite structure transition is possible for nanosized ZnS using modifiers, and these authors also have reported water-driven structure transformation in nanoparticles at room temperature. Within this framework, achievement of suitable control of the phase transition behavior of nanometer-sized ZnS materials would represent a significant progress on the way to their full exploitation in different areas of science and engineering.

In recent years, well defined ZnS nanoparticles with various morphologies and structures, including nanotubes, nanorods, nanowires, nanocubes, nanospheres, nanoflowers and nanosheets, have been successfully synthesized and studied using a variety of methods, [9,24-31]. In addition to these techniques, the preparation of ZnS via solution chemical routes provides a promising option for the large-scale production of this material. Therefore, it is important to develop new environmentally friendly processing material methods with low costs, and with the possibility of formation of nanoscale materials with phase control and well-defined morphologies. Developing this phase-selective synthesis, in general, is crucial for the design of ZnS nanocrystals with novel tunable physical properties is of great interest in nanotechnology.

The synthesis route of nanoparticles has a major influence on their size, shape and optical properties. Recently, microwave-assisted procedure has been developed into an efficient method for the fabrication of nanomaterials, and is becoming very attractive in all areas of synthetic chemistry because it has some advantages over other synthetic methods [32,33], because the application of microwave irradiation on chemical transformations often results in dramatic rate accelerations, enhanced yields, cleaner reactions [32-36] and improved material quality and size distributions in nanomaterials [34-40]. Some comprehensive reviews on microwave-assisted syntheses of nanomaterials have been published [37,41].

The mechanism associated with microwave effects in synthesis are not well understood [38,42,43], and this is an open research field. In such cases, it is certain that quantum chemistry tools are extremely helpful in the rationalization and interpretation of reaction mechanisms at the atomic level, based on the characterization of key intermediates along the reaction pathways.

Here we report a rapid and economical microwave-assisted route for the preparation and phase control of ZnS nanoparticles by a simple microwave-assisted solvothermal (MAS) method and the presence of tetrabutylammonium hydroxide. The formation mechanism and the conditions under which the phase of the as-synthesized ZnS (wurtzite and zinc blende) are obtained and discussed in detail. The obtained materials were analyzed by X-ray diffraction (XRD), field emission scanning electron microscopy (FE-SEM), energy dispersive X-ray spectroscopy (EDXS), ultraviolet–visible (UV–vis) and photoluminescence (PL) measurements. Targeting a better understanding of the experimental data, theoretical calculations were carried out by time-dependent density functional theory (TDDFT). In addition, this study gives practical guidance for controlling the phase in MAS growth of ZnS nanostructures and the effects as well as the merits of microwave heating on the process and characteristics of the obtained ZnS powders are reported.

2. Methodology

2.1 Materials

All reagents were analytical grade and were used without further purification. ZnS nanostructures were synthesized by the MAS method with or without modifier assistance, in the presence of ethylene glycol (EG) at 140 °C and for short times.

In a typical procedure, 7.34 mmol of zinc acetate are dissolved into 25 mL of EG and heated to 80 °C (solution 1); 7.34 mmol of thiourea is separately dissolved into another 25 mL of EG (solution 2). With vigorous magnetic stirring, solution 1 is then quickly injected into solution 2. In the sequence, the solution was transferred into a Teflon autoclave, which was sealed and placed inside a domestic microwave-solvothermal system (2.45 GHz, maximum power of 800 W). The microwave-solvothermal processing was performed at 140 °C for 10 min. The resulting precipitate was washed with deionized water and ethanol to remove byproducts possibly remaining in the final product and the precipitates were finally collected and dried at 70 °C overnight. The synthesis was also performed with the assistance of a modifier. For this we conducted the same procedure described above with the addition of 15.44 mmol of tetrabutylammonium hydroxide (40%) in solution 1.

2.2 Characterization

The obtained powders were structurally characterized by XRD using a Rigaku-DMax/2500PC with Cu K α radiation (λ = 1.5406 Å) in the 2θ range from 10° to 75° with 0.02°/min. The phase analysis

by the Rietveld method [44] was carried out using the *General Structure Analysis System* (GSAS) software [45].

The morphologies of ZnS powder were observed by FE-SEM using FEG-VP JEOL. The compositional analysis as well as the mapping of the elements in the analyzed samples was performed by means of energy dispersive X-ray spectroscopy (EDXS). Optical properties were analyzed by means of UV-vis absorption spectra using a Cary 5G spectrophotometer (Varian, USA) in a diffuse reflection mode.

2.3 Computational Details and Model Systems

All calculations were carried out using the Gaussian 09 program package [46]. The structures of the reactants, intermediates, and products along the growth mechanism for the model systems have been fully optimized by TDDFT with the B3LYP functional [47,48] employing the standard all-electron 6-311+G (d,p) basis set to describe the atoms. No imaginary frequencies were found for the optimized geometries. The solvent effect was evaluated with utilization of polarized continuum model (PCM) [49,50], using a dielectric constant of 41.4 to simulate the EG.

Two model systems: Zn_4S_4 and Zn_6S_6 clusters have been selected to represent the cubic zinc blende and the hexagonal wurtzite, respectively (see Figure 1). For the Zn_4S_4 and Zn_6S_6 clusters, the local structure, excitation energy and oscillator strength for electronic transitions from the ground to excited states have been obtained by means TDDFT calculations using 6-311+G (d,p) basis set. Molecular orbitals (MO) picture were prepared using the Gaussian View 2.1 package [46] using a contour value of 0.030 and project density of states (DOS) was analyzed using GaussSum [51].

(Figure 1)

To understand the role of modifier in the synthesis, i.e. tetrabutylammonium hydroxide, the interaction energy with the surface of both Zn_4S_4 and Zn_6S_6 clusters has been obtained, following the Equation 1:

$$\Delta E_{inter} = E_{A/B} - E_A - E_B \quad (1)$$

where ΔE_{inter} is the interaction energy, $E_{A/B}$ is the total energy calculated for the modifier molecule adsorbed on the surface of Zn_4S_4 or Zn_6S_6 clusters, E_A is the energy of the modifier molecule and E_B is the energy of the clusters.

2. Results and discussion

Figure 2 depicts the XRD patterns, showing that the samples processed with the MAS method are highly crystalline, pure and ordered at long range. All diffraction peaks of ZnS nanoparticles can be indexed to the hexagonal structure or cubic structure in agreement with the respective Joint Committee on Powder Diffraction Standards (JCPDS) cards 36−1450 and 80-20 [52,53]. No other diffraction peaks are found, which indicates that the products are pure ZnS.

(Figure 2.)

The diffraction peaks are significantly broadened because of the very small crystallite size. The mean of size crystallites, T, was calculated from the Scherrer equation (eq. 2) [54]:

$$T = \frac{0.9\lambda}{\beta \cos\theta} \quad (2)$$

where λ is the K_α radiation; θ is the Bragg diffraction angle; and β is the width of the peak at half the maximum intensity in radians (Table 1). The strain and grain size of the both samples were calculated by Williamson–Hall (W-H) method, according to the following equation (eq. 3) [55]. In particular, the W–H analysis is a simplified integral breadth method where strain-induced broadening arising from crystal imperfections and distortion in the lattice [56-58]. Thus, the full width at half maximum (FWHM) may be expressed in terms of strain (ε) is estimated from the slope of the line and the crystallite size (T) from the intersection with the vertical axis and other parameters have the same meaning as in eq. 2. The W–H plot for of ZnS nanoparticles obtained by MAS method is shows in Figure 3 (b,d).

$$\frac{\beta \cos\theta}{\lambda} = \frac{0.9}{T} + \frac{\varepsilon \sin\theta}{\lambda} \quad (3)$$

(Table 1.)

In order to prove that compounds obtained by the MAS method are pure and feature single-phase was employed the Rietveld refinement method in this study, with the specific objective to

analyze and understand whether there are differences in the structural arrangements and for determining the size of the particles of ZnS nanoparticles obtained by MAS method (see Figure 3(a,c)).

(Figure 3)

From Rietveld analysis, fitting parameters (R_{WP}, R_p, R_{exp} *and* χ^2) indicate good agreement between refined and observed XRD patterns for the samples obtained by the MAS method (see Table 2). These phases corresponding to the different polymorphs of the ZnS can be are clearly identified in this case, it was noted that the lattice parameters and unit cell volumes obtained for both zinc blende and wurtzite of the ZnS structures are very close to those published in the literature [58,59]. However, some variations in the atomic positions related to sulfur atoms were observed while zinc atoms have fixed atomic positions. These results indicate certain degree of disorder for the samples obtained by the MAS method, especially the sulfur vacancies. We believe these variations in atomic positions of sulfur atoms can lead to the formation types of distortions on [S–Zn–S] bonds and consequently promotes different levels of distortions on the [ZnS_4] and/or [ZnS_3] clusters in the lattice of ZnS.

(Table 2.)

Our results clearly correspond to two different growth rates for two different directions, implying an irregular spherical-like particle shape promoting a simple way to phase control of ZnS nanoparticles during processing in the MAS conditions, on the other hand, the reaction yields much more hexagonal phase than the cubic phase. These results indicate that the crystal phase of ZnS prepared by MAS synthesis can be controlled by adjusting experimental parameters mediated by the presence of tetrabutylammonium hydroxide (see Figure 2).

The FE-SEM micrographs in Figure 4 illustrate the influence of the different preparation conditions on the morphology and size distribution of the prepared samples. FE-SEM images show that the synthesis route produces ZnS crystalline agglomerate nanoparticles as can be observed on the ZnS particles facets are quite similar, as shown in Figure 4 (a-b). The interface characteristics and growth are strongly driven by the chemistry of the surface, which in turn contributes to the phase stability [17,61-63].

(Figure 4.)

Microwave processing provides rapid formation of a high density of nucleation sites and the growth of the ZnS nanoparticles. These nanocrystals have a strongly polarized surface, because of a high concentration of short and intermediate-range defects. In previous studies [9], we suggested that the growth of the ZnS obtained by MAS can be described via nucleation-dissolution-recrystallization mechanism, and these mechanisms are responsible for the fast nucleation of the ZnS small particles which aggregate into a spherical morphology to minimize their surface energy. In general, the nucleation-dissolution-recrystallization mechanism occurs using the MAS method [9,38,40,64], which is considered highly sensitive to relative rates of amorphous solid particle dissolution and nucleation of the crystalline phase [17,38,64-68]. As a consequence, this mechanism involves the formation of a high concentration of aggregated nanoparticles with predominant growth controlled by the coalescence process [39]. EDXS reveals that the products contain Zn and S which is in excellent agreement with the stoichiometry of ZnS, indicating the purity of sample processed by MAS method. The EDXS spectra are also very similar to the spectrum of ZnS published by Ludi et al [69].

In recent years, considerable effort has been devoted to the synthesis of nanocrystals prepared by a solvothermal process using various modifiers to control and induce the growth of nanocrystals [39,70-78]. The modifier plays a different role in each type of synthesis, and their effects are not completely understood. The use of a modifier in the chemical synthesis of nanomaterials has been employed to obtain new shapes with different sizes, which promotes the formation of materials with different chemical behaviour [76-78].

According to Lamer and Dinegar [79], the precursor conversion reactions that limit the crystallization determines the temporal evolution of monomer concentration as well as the steady state supersaturation during the growth phase. In our case, the $[Zn(SH)_4]^{2-}$ complex in solution can be considered as the growth unit for the ZnS nanostructures [80-82]. Therefore, we propose a growth process of ZnS nanostructures as shown in Figure 5, and to further understand the phase control, cubic zinc blende vs. hexagonal wurtzite , we use of the Zn_4S_4 and Zn_6S_6 clusters as model systems (see Figure 1). These clusters serve as a base for the growth of larger crystals, and have been experimentally characterized by mass spectrometry [83]. The Zn-S distances calculated are 2.38 and 2.32/2.42 Å for the cubic zinc blende Zn_4S_4 and hexagonal wurtzite Zn_6S_6 clusters, respectively, which are in good agreement with other

theoretical studies [83-88]. It is important to note that the experimental values of the lattice parameters reported for the bulk ZnS structures, exhibit Zn-S bonding distances that are quite similar for wurtzite and zinc blende (~ 2.34 Å), due the great similarity in the local coordination of the tetrahedral [ZnS_4] cluster in the lattice [89].

(Figure 5)

The theoretical infrared- and Raman-active modes for the Zn_4S_4 and Zn_6S_6 clusters are shown in the Figure 6. An analysis of the results yields two and five active infrared lines, while four and seven active lines in the Raman spectra are found for the Zn_4S_4 and Zn_6S_6 clusters, respectively.

(Figure 6.)

The condensation of these complexes occurs through a mechanism of nucleophilic substitution, in which two original zinc complexes or monomers are found in the solution and react to form a dimer, with elimination of H_2S and form a sulfur bridges (intermediate II) [Zn-S-Zn] with stronger chemical bonds,. From this intermediate II, there are two possible reaction pathways: (i) the intramolecular cyclic rearrangement of this dimer to form a cyclic structure, intermediate III, or (ii) the formation of a trimer, intermediate IV. This second step can be associated to the phase control along the growth process of ZnS nanocrystals. We have estimated differences in Gibbs free energies to study the reaction mechanism. This, however, is a crude approximation because medium effects are not taken into account. An analysis of the results shows that the reaction pathway for the formation at the nanoscale of ZnS suggests that the formation of the trimer (intermediate III) is more favorable energetically about 156.59 kcal/mol relative to form a cyclic structure (intermediate IV). Thus, based on these results we can show that the hexagonal wurtzite phase is more favorable energetically with respect to cubic zinc blende from a thermodynamic point of view in nanoscale.

With respect to structures shown in Figure 1, Zn_4S_4 cluster has only one type of Zn atom, while the hexagonal phase (Zn_6S_6 cluster) contains two different Zn atoms in this cluster that can be thought of as the unit cell of a wurtzite structure. More recently, a benchmark data set using DFT and TDDFT of geometrical parameters, vibrational normal modes, and low-lying excitation energies for these clusters have been reported by Azpiroz et al [88].

The calculated values of the interaction energy of the modifier molecule, tetrabutylammonium hydroxide, on the surface of Zn_6S_6 (with the active sites A and B) and Zn_4S_4 clusters and the corresponding optimized geometries are given in Table 3. An analysis of the results shows that the value of the interaction energies of the modifier are energetically favorable, at the A (-87.27 kcal.mol^{-1}) and B (-94.23 kcal.mol^{-1}) sites which are more favorable in the Zn_6S_6 cluster than in the Zn_4S_4 cluster (-30.87 kcal.mol^{-1}). In particular, theoretical calculations on the relative stability of both phases of the bulk ZnS has been previously studied by Yeh et al [90]. This result can explain that the tetrabutylammonium hydroxide modifier favors the formation of hexagonal wurtzite phase with respect to the cubic phase.

(Table 3.)

According to the literature [9,39], the ZnS exhibits an optical absorption spectrum governed by direct electronic transitions. UV–Vis diffuse reflectance was used to determine the band gap of these materials in order to better understand the differences in ZnS nanostructures (see Figure 7(a-b)). The Kubelka–Munk method based on diffuse reflectance spectra was employed to determine the band gap of these materials [9]. UV-vis absorption measurements illustrate a variation in the optical band gap values from 3.40 to 3.59 eV for ZnS nanoparticles, for the zinc blende structure and wurtzite structure, respectively. After the electronic absorption process, electrons located in the maximum-energy states in the valence band revert to minimum-energy states in the conduction band under the same point in the Brillouin zone [39]. In particular, the band gap values obtained for the samples are much lower than the expected for the band gap values of 3.68 eV for the zinc blende and 3.77 eV for the wurtzite, respectively for the bulk ZnS reported by Fang et al [2]. The exponential optical absorption edge and the optical band gap energy are controlled by the degree of structural disorder in the lattice [9,39,40]. The decrease in the band gap value can be attributed to defects and local bond distortion as well as intrinsic surface states and interfaces which yield localized electronic levels within the forbidden band gap, due to electron transitions from the valence band to the conduction band.

(Figure 7.)

Figure 7(c-d), show PL evolutions of ZnS samples synthesized by a MAS method with or without any modifier assistance at 140 °C. The PL spectra for ZnS samples present a broad band covering the visible electromagnetic spectra in the range from 400 to 800 nm, with maximum emission at 485 and 530 nm, for the hexagonal structures and cubic structures respectively, when excited by a 350.7 nm laser line. This behavior is due to changes in shape, crystal size, structure and orientation of ZnS crystals. The emission band profile is typical of a multiphonon process; i.e., a system where relaxation occurs by several paths involving the participation of numerous states within the band gap of the material [9,39]. In this scenario, we have investigated the electronic structure of the cubic zinc blende Zn_4S_4 and hexagonal wurtzite Zn_6S_6 clusters using the frontier molecular orbitals obtained from TDDFT calculations.

(Figure 8.)

Figure 8 shows the shape of molecular orbitals calculated for the Zn_4S_4 and Zn_6S_6 clusters. The HOMO–LUMO gaps calculated and experimental values in parentheses are 3.16 (3.40) and 3.88 (3.59) eV for the Zn_4S_4 and Zn_6S_6 clusters, respectively [83-88], while the values of the energy of first ionization potentials (IPs), calculated in the framework of Koopmans' theorem [91] are 7.15 and 6.95 eV for the Zn_4S_4 and Zn_6S_6 clusters, respectively. An analysis of the DOS for the cubic Zn_4S_4 and hexagonal Zn_6S_6 clusters shows that the HOMO orbital consists mainly of S 3*p* orbitals whereas the LUMO is composed by Zn 4*sp* hybrid orbitals (see Figure 8).

4. Conclusions

In summary, we have demonstrated phase control, mediated by the presence of tetrabutylammonium hydroxide, in the growth of ZnS crystal that by using a low cost effectiven MAS method, a very moderate temperature (140 °C) and a very fast reaction time are sufficient to produce nanostructures with good degree of crystallinity. XRD, FE-SEM, EDXS measurements and theoretical calculations were extensively employed to investigate structural, and surface chemical compositions along the growth process of the synthesized nanostructures. Our results strongly suggest that the crystal phase of the prepared ZnS can be controlled by a modifier, i.e. tetrabutylammonium hydroxide and a new route has opened up for constructing novel nanostructures, which gives a better understanding of the control of ZnS nanostructures and their optical behaviour at the atomic-level. This finding offers new possibilities and shows that theory can be a suitable partner with experiments in developing and rationalizing these properties at the atomic level which is very important for progress in nanotechnology.

Acknowledgements

The authors gratefully acknowledge the support of the Brazillian agencies FAPESP, CNPq and CAPES. J.A. also acknowledges Generalitat Valenciana for Prometeo/2009/053 project, Ministerio de Economia y Competitividad (Spain) under project CTQ2012-36253-C03-02, and Programa de Cooperación Científica con Iberoamerica (Brasil), Ministerio de Educación (PHB2009-0065-PC). Special appreciation is extended to Dr D. P. Volanti for the development of the MAS method.

Notes and references

[a] Instituto de Química, UNESP, PO Box 355, 14801-970, Araraquara, SP, Brazil.
[b] Department of Analytical and Physical Chemistry, Univ Jaume I, Castelló de la Plana, 12071, Spain.
[c] Departamento de Física, USP, PO Box 369, 13560-970 São Carlos, São Paulo, Brazil.
[d] Laboratório de Simulação Molecular, UNESP, PO Box 473, 17033-360 Bauru, SP, Brazil.
† *Corresponding author:*
Email: felipe_laporta@yahoo.com.br;
Phone: +55 16 3301-9892; Fax: +55 16 3301-9691

1. Y. C. Cao and J. Wang, *J. Am. Chem. Soc.*, 2004, **126**, 14336.
2. X. Fang, T. Zhai, U. K. Gautam, L. Li, L. Wu, Y. Bando and D. Golberg, *Prog. Mater. Sci.* 2011, **56**, 175
3. X. Wang, J. Shi, Z. Feng, M. Li and C. Li, *Phys. Chem. Chem. Phys.*, 2011,**13**, 4715.
4. A. K. Kole, C. S.Tiwary and P. Kumbhakar, *CrystEngComm*, 2013, **15**, 5515.
5. F.-J. Fan, L. Wu and S.-H. Yu, Energy Environ. Sci., 2014, 7, 190.
6. Y. G. Zhang, G. Y. Wang, X. Y.Hu, Q.F.Shi, T. Qiato and Y. Yang, *J. Cryst. Growth*, 2005, **284**, 554.
7. N. S. N. Jothi and P. Sagayaraj, *Arch. Appl. Sci. Res.*, 2012, **4**, 1079.
8. F. A. La Porta, L. Gracia, J. Andrés, J. R. Sambrano, J. A. Varela and E. Longo, *J. Am. Ceram. Soc.*, 2014, in press.
9. F. A. La Porta, M. M. Ferrer, Y. V. B. Santana, C. W. Raubach, V. M. Longo, J. R. Sambrano, E. Longo, J. Andrés, M. S. Li and J. A. Varela, *J. Alloys Compd.*, 2013, **556**, 153.
10. P. K. Giri, D. K. Goswani, A. Perumal, Advanced Nanomaterials and Nanotechnology, Springer-Verlag Berlin Heidelberg, 2013, pp. 66.

11. Y. Zhao, Y. Zhang, H. Zhu, G.C. Hadjipanayis and J.Q. Xiao, *J. Am. Chem. Soc*. 2004, **126**, 6874.
12. F. Huang and J.F. Banfield, *J. Am. Chem. Soc*. 2005, **127**, 4523.
13. J.Q. Sun, X.P. Shen, K.M. Chen, Q. Liu, W. Liu, *Solid State Commun.* 2008, **147**, 501.
14. H. Tong, Y.J. Zhu, L.X. Yang, L. Li, L. Zhang, J. Chang, L.Q. An, S.W. Wang, *J. Phys. Chem. C* 2007, **111**, 3893.
15. S. A. Acharya, N. Maheshwari, L. Tatikondewar, A. Kshirsagar, and S. K. Kulkarni, *Cryst. Growth Des*. 2013, **13**, 1369.
16. J. Zhang, Z. Lin, Y. Lan, G. Ren, D. Chen, F. Huang and M. Hong, *J. Am. Chem. Soc*. 2006, **128**, 12987.
17. De Yoreo, J. J.; Vekilov, P. G. In ReViews in Mineralogy and Geochemistry: Biomineralization; Dove, P. M., De Yoreo, J. J., Weiner, S., Eds.; Mineralogical Society of America: Washington, DC, 2003; Vol. 54, p 57.
18. F. C. Meldrum and H. Cölfen, *Chem. Rev.* 2008, **108**, 4332.
19. C. A. Feigl, A. S. Barnard and S. P. Russo, *Phys. Chem. Chem. Phys.*, 2012, **14**, 9871.
20. C. A. Feigl, S. P. Russo and A. S. Barnard, *J. Mater. Chem*., 2010, **20**, 4971.
21. O. Brafman and S. S. Mitra, *Phys. Rev.* 1968, **171**, 931
22. Y. Ding, X. D. Wang and Z. L. Wang, *Chem. Phys. Lett.* 2004, **398**, 32.
23. H. Zhang, B. Gilbert, F. Hung and J. F. Banfield, *Nature*, 2003, **424**, 1025.
24. Y. Chen, Q.-S. WuI and Y.-P. Ding, *J. Braz. Chem. Soc.* 2007, **18**, 924.
25. L. S. Li, N. Pradhan, Y. Wang and X. Peng, *Nano Lett.*, 2004, **4**, 2261.
26. J. Joo, H. B. Na, T. Yu, J. H. Yu, Y. W. Kim, F. Wu, J. Z. Zhang and T. Hyeon, *J. Am. Chem. Soc.*, 2003, **125**, 11100.
27. A. K. Kole, C. S. Tiwary and P. Kumbhakar, *J. Mater. Chem. C*, 2014, **2**, 4338.
28. J. Kennedy, P. P. Murmu, P. S. Gupta, D. A. Carder, S. V. Chong, J. Leveneur and S. Rubanov, *Mater. Sci. Semicond. Process.*, 2014, **26**, 561.
29. C. S. Pathak, M. K. Mandal, D. D. Mishra and V. Agarawala, *J. Adv. Microsc. Res.*, 2013, **8**, 222.
30. X. Huang, M.-G. Willinger, H. Fan, Z.-L. Xie, L. Wang, A. Klein-Hoffmann, F. Girgsdies, C.-S. Lee and X.-M. Meng, *Nanoscale*, 2014, in press.
31. Y. S. Jang and Y. C. Kang, *Phys. Chem. Chem. Phys.*, 2013,**15**, 16437.
32. T. N. Glasnov and C. O. Kappe, *Chem.–Eur. J.*, 2011, **17**, 11956.
33. H. Katsuki and S. Komarneni, *J. Ceram. Soc. Jpn.*, 2011, **119**, 525.
34. H.-Q. Wang and T. Nann, *ACS Nano*, 2009, **3**, 3804.
35. G. B. Dudley, A. E. Stiegman and M. R. Rosana, *Angew. Chem., Int. Ed*., 2013, **52**, 7918.
36. I. Bilecka and M. Niederberger, *Nanoscale*, 2010, **2**, 1358.
37. M. Baghbanzadeh, L. Carbone, P. D. Cozzoli and C. O. Kappe, *Angew. Chem., Int. Ed*., 2011, **50**, 11312.
38. T. A. Mulinari, F. A. La Porta, J. Andrés, M. Cilense, J. A. Varela and E. Longo, *CrystEngComm*, 2013, **15**, 7443.
39. Y. V. B. Santana, C. W. Raubach, M. M. Ferrer, F. La Porta, J. R. Sambrano, V. M. Longo, E. R. Leite and E. Longo, *J. Appl. Phys.*, 2011, 110, 123507.
40. V. M. Longo, L. S. Cavalcante, E. C. Paris, J. C. Sczancoski, P. S. Pizani, M. S. Li, J. Andrés, E. Longo and J. A. Varela, *J. Phys. Chem. C* 2011, **115**, 5207.
41. Y.-J. Zhu and F. Chen, *Chem. Rev.* 2014, in press (DOI: 10.1021/cr400366s).
42. D. Dallinger and C. O. Kappe. *Chem. Rev.* 2007, **107**, 2563.
43. L. Pan, X. Liu, Z. Sun and C. Q. Sun, *J. Mater. Chem. A*, 2013, 1 (29), 8299.
44. H. M. Rietveld, *J. Appl. Crystallogr.*, 1969, **2**, 65.
45. A. C. Larson and R. B. Von Dreele, General Structure Analysis System (GSAS), Los Alamos National Laboratory Report LAUR, 1994, vol. 86, p. 748.
46. M. Frisch, et al. Gaussian 09, Revision B.01, Gaussian Inc.: Wallingford, CT, 2010.
47. A. D. Becke, *J. Chem. Phys.* 1993, **98**, 5648.
48. C. Lee, W. Yang and R. G. Parr, *Phys. Rev. B*. 1988, **37**, 785.
49. S. Miertus, E. Scrocco and J. E. Tomasi, *J. Chem. Phys.* 1981, **55**, 117.
50. S. Miertus, *Chem. Phys.* 1982, **65**, 239.
51. N. M. O'Boyle, A. L. Tenderholt and K. M. Langner, *J. Comp. Chem*., 2008, **29**, 839.
52. JCPDS File No. 36−1450
53. JCPDS File No. 80-20
54. A. Guinier, X-rays diffraction in crystals, imperfect crystals, and amorphous bodies, San Francisco, W. H. Freeman, USA, 1963.
55. C. Suryanarayana and M. G. Norton, X-ray Diffraction: A Practical Approach. Springer, New York (1998).
56. R. Kripal, A. K. Gupta, S. K. Mishra, R. K. Srivastava, A. C. Pandey and S. G. Prakash, *Spectrochim. Acta Part A*, 2010, **76**, 523.
57. V. D. Mote, Y. Purushotham, B. N. Dole, *Journal of Theoretical and Applied Physics* 2012, **6**, 6.
58. A. K. Kole and P. Kumbhakar, *Results in Physics,* 2012, **2**, 150.
59. G. O. Siqueira, T. Matencio, H. V. da Silva, Y. G. de Souza, J. D. Ardisson, G. M. de Lima and A. O. Porto, *Phys. Chem. Chem. Phys.* 2013, 15, 6796.
60. (a) B. K. Agrawal, P. S. Yadav and S. Agrawal, *Phys. Rev. B: Condens. Matter.* 1994, **15**, 14881; (b) E. H. Kisi and M. M. Elcombe, *Acta Cryst.* 1989, C**45**, 1867.
61. E. R. Leite, T. R. Giraldi, F. M. Pontes, E. Longo, A. Beltrán and J. Andrés, *Appl. Phys. Lett.*, 2003, **83**, 8, 1566.
62. H. Zheng, R. K. Smith, Y.-W. Jun, C. Kisielowski, U. Dahmen and A. P. Alivisatos, *Science*, 2009, **324**, 1309.
63. A. Elsen, S. Festersen, B. Runge, C. T. Koops, B. M. Ocko, M. Deutsch, O. H. Seeck, B. M. Murphy and O. M. Magnussen, *Proc. Natl. Acad. Sci.*, 2013, **110**, 6663.
64. Z. J. Luo, H. M. Li, H. M. Shu, K. Wang, J. X. Xia and Y. S. Yan, *Cryst. Growth Des.* 2008, **8**, 2275.
65. R.-Q. Song and H. Cölfen, *Adv. Mater*., 2010, **22**, 1301.
66. H. Cölfen and M. Antonietti, Mesocrystals and Nonclassical Crystallization., JohnWiley & Sons Ltd, Chichester, UK, 2008.
67. L. Zhou and P. O'Brien, *J. Phys. Chem. Lett.*, 2012, **3**, 620.

68. H. Cölfen and M. Antonietti, *Angew. Chem., Int. Ed*., 2005, **44**, 5576.
69. B. Ludi, I. Olliges-Stadler, M. D. Rossell and M. Niederberger, *Chem. Commun.* 2011, **47**, 5280.
70. M. Rajamathia, R. Seshadri, *Curr. Opin. Solid State Mater. Sci.* 2002, **6**, 337.
71. G. Zou, H. Li, Y. Zhang, K. Xiong and Y. Qian, *Nanotechnology*, 2006, **17**, S313.
72. T. He, D. Chen, X. Jiao, Y. Xu and Y. Gu, *Langmuir*, 2004, **20**, 8404.
73. C. Zhang, Z. Kang, E. Shen, E. Wang, L. Gao, F. Luo, C. Tian, C. Wang and Y. Lan, *J. Phys. Chem. B*, 2006, 110, 184.
74. Q. Zhao, L. Hou and R. Huang, *Inorg. Chem. Commun*., 2003, **6**, 971.
75. A. K. Shahi, B. K. Pandey, R. K. Swarnkar and R. Gopal, *Appl. Surf. Sci.* 2011, **257**, 9846.
76. M. A. P. Almeida, L. S. Cavalcante, J. A. Varela, M. S. Li and E. Longo, Adv. Powder Technol., 2012, **23**, 124.
77. L. S. Cavalcante, J. C. Sczancoski, M. S. Li, E. Longo and J. A. Varela, *Colloids Surf., A*, 2012, **396**, 346.
78. M. R. D. Bomio, R. L. Tranquilin, F. V. Motta, C. A. Paskocimas, R. M. Nascimento, L. Gracia, J. Andres and E. Longo, *J. Phys. Chem. C*, 2013, **117**, 21382.
79. V. K. Lamer and R. H. Dinegar, *J. Am. Chem. Soc.,* 1950, **72**, 4847.
80. C. R. A. Catlow, S. T. Bromley, S. Hamad, M. Mora-Fonz, A. A. Sokol and S. M. Woodley*, Phys. Chem. Chem. Phys*., 2010, **12**, 786.
81. D. L. Golic, Z. Brankovic, N. Daneu, S. Bernik and G. Brankovic, *J. Sol-Gel Sci. Technol.,* 2012, **63**, 116.
82. J. A. Tossell and D. J. Vaughan, *Geochim. Cosmochim. Ac.* 1993, **57**, 1935.
83. A. Burnin, E. Sanville and J. J. BelBruno, *J. Phys. Chem. A* 2005, **109**, 5026.
84. J. M. Azpiroz, X. Lopez, J. M. Ugalde and I. Infante, *J. Phys. Chem. C*, 2012, **116**, 4, 2740.
85. M. Zwijnenburg, F. Illas and S. T. Bromley, *Phys. Chem. Chem. Phys*., 2011, **13**, 9311.
86. J. M. Azpiroz, E. Mosconi, F. De Angelis, *J. Phys. Chem. C* 2011, **115**, 25219.
87. M. Zwijnenburg, C. Sousa, F. Illas and S. T. Bromley, *J. Chem. Phys*., 2011, **134**, 064511.
88. J. M. Azpiroz, J. M. Ugalde and I. Infante, J. Chem. Theory Comput., 2014, 10, 76
89. Y. R. Wang and C. B. Duke, *Phys. Rev. B*., 1987, **36**, 2763.
90. C. Y. Yeh, Z. W. Lu, S. Froyen and A. Zunger, *Phys. Rev. B*, 1992, **46**,10086.
91. T. A. Koopmans, Physica 1933, **1**, 104.

Figure Captions:

1. **Figure 1:** Geometry of the ZnS clusters. (a) Zn_4S_4 and (b) Zn_6S_6 clusters have been selected to represent the cubic zinc blende and the hexagonal wurtzite, respectively
2. **Figure 2:** (A) A schematic representation of the synthesis of ZnS nanostructures (cubic versus hexagonal) by means of the microwave-assisted solvothermal method, in which the phase control is provided by the modifier (tetrabutylammonium hydroxide) (B) XRD patterns of ZnS nanostructures at 140 °C.
3. **Figure 3:** Williamson–Hall analysis and Rietveld refinement plot of ZnS nanoparticles processed by MAS at 140 °C: (a-b) Zinc blende and (c-d) Wurtzite.
4. **Figure 4:** FEG-SEM images, EDS patterns and particle size distribution for (left) cubic and (right) hexagonal ZnS nanostructures.
5. **Figure 5:** Proposed intermediates along the reaction pathways to obtain cubic and hexagonal ZnS nanostructures.
6. **Figure 6:** Theoretical vibrational modes, (a) Infrared and (b) Raman, obtained at B3LYP/6-31+G calculation level for Zn_4S_4 and Zn_6S_6 cluster models
7. **Figure 7:** Optical properties of both cubic and hexagonal ZnS nanostructures: (A and B) Normalized PL spectra at room temperature, (C and D) UV-vis spectra and (E) Schematic representation of the optical property involving fundamental and excited electronic states.
8. **Figure 8:** Representation of the frontier molecular orbitals representation and projected DOS obtained TDDFT calculation level: (a) cubic zinc blende Zn_4S_4 cluster and (b) hexagonal wurtzite Zn_6S_6 cluster.
9. **Figure 9:** Optimized structures involving the interaction of a modifier molecule ((tetrabutylammonium hydroxide) with ZnS clusters in different active sites of Zn atoms. (a) Zn_6S_6 site A, (b) Zn_6S_6 site B and (c) Zn_4S_4 clusters.
10. **Table 1:** Crystallite size and reaction yield of ZnS nanostructures with or without any modifier assistance at 140 °C.
11. **Table 2:** Rietveld refinement results for the ZnS nanoparticles.
12. **Table 3:** Selected geometrical parameters and values of the interaction energy (ΔE_{inter}) between the modifier molecule and the different ZnS cluster models.

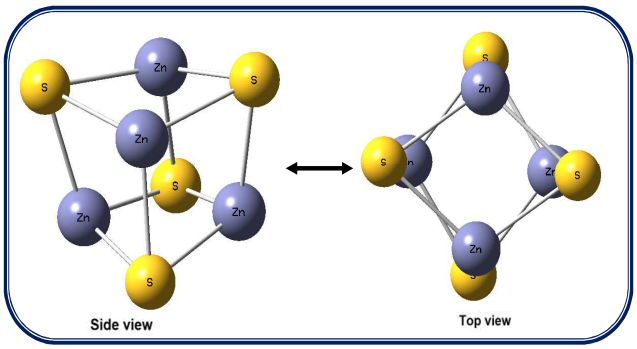

(a)

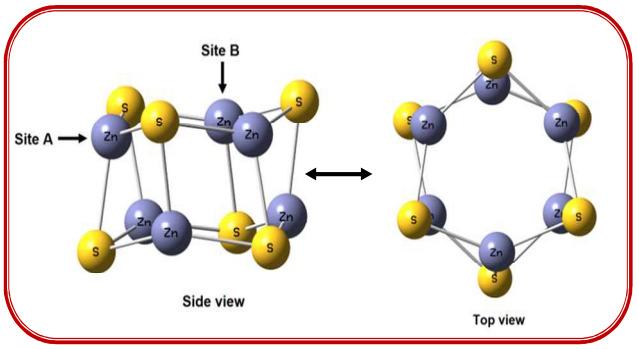

(b)

Figure 1.

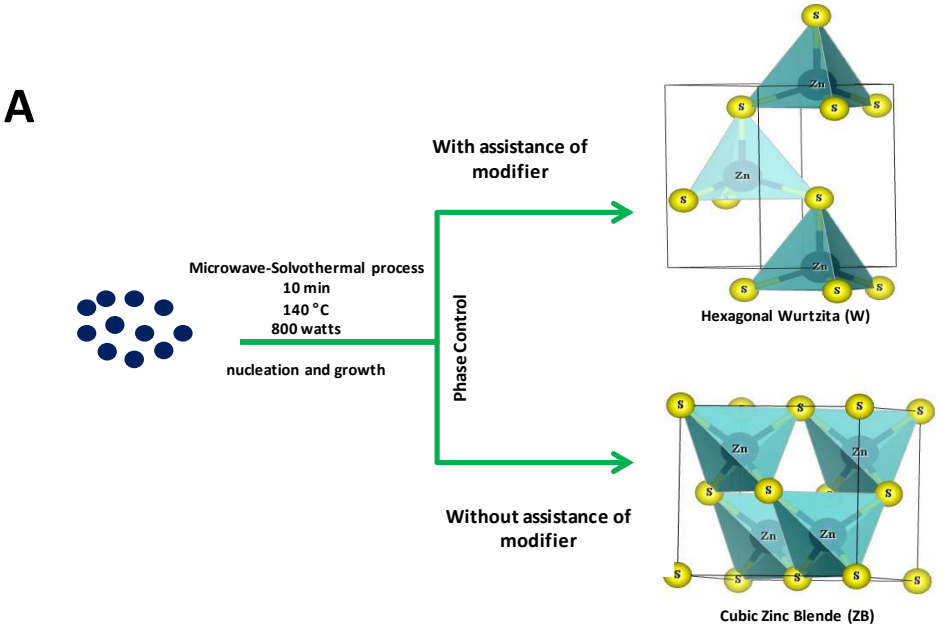
A
With assistance of modifier
Microwave-Solvothermal process
10 min
140 °C
800 watts
nucleation and growth
Phase Control
Hexagonal Wurtzita (W)
Without assistance of modifier
Cubic Zinc Blende (ZB)

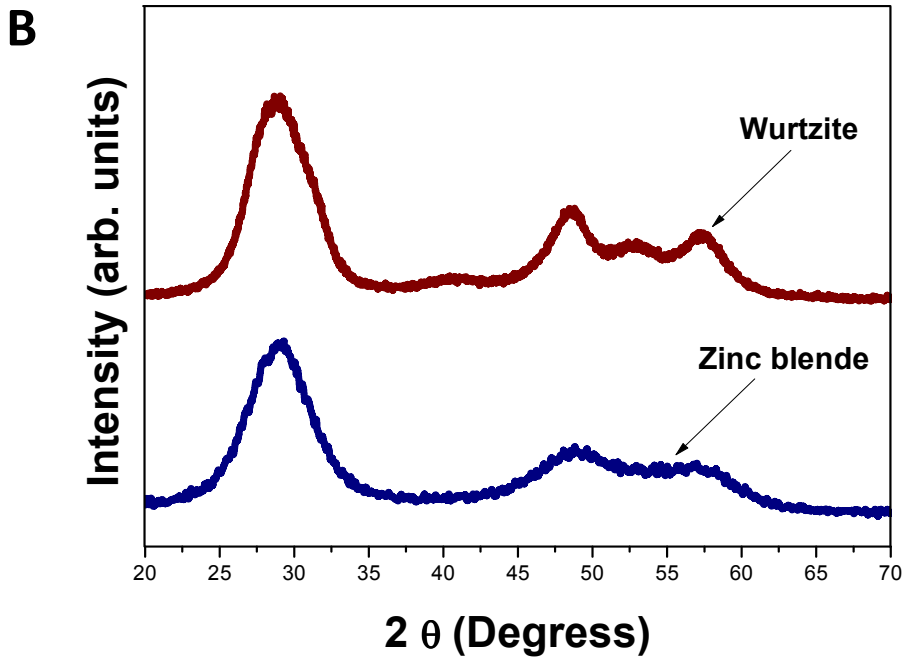
B
Intensity (arb. units)
Wurtzite
Zinc blende
20
25
30
35
40
45
50
55
60
65
70
2 θ (Degress)

Figure 2.

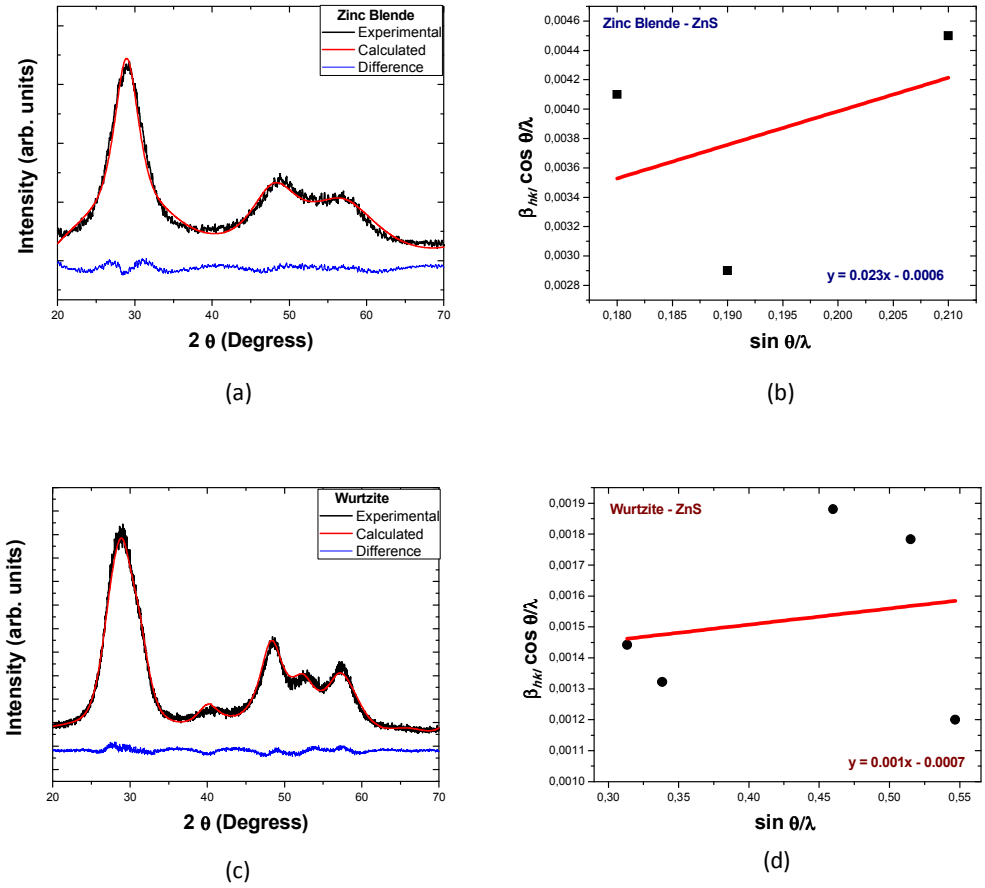
Zinc Blende
Experimental
Calculated
Difference
Intensity (arb. units)
2 θ (Degress)
(a)
Zinc Blende - ZnS
β_{hkl} cos θ/λ
y = 0.023x - 0.0006
sin θ/λ
(b)
Wurtzite
Experimental
Calculated
Difference
Intensity (arb. units)
2 θ (Degress)
(c)
Wurtzite - ZnS
β_{hkl} cos θ/λ
y = 0.001x - 0.0007
sin θ/λ
(d)

Figure 3.

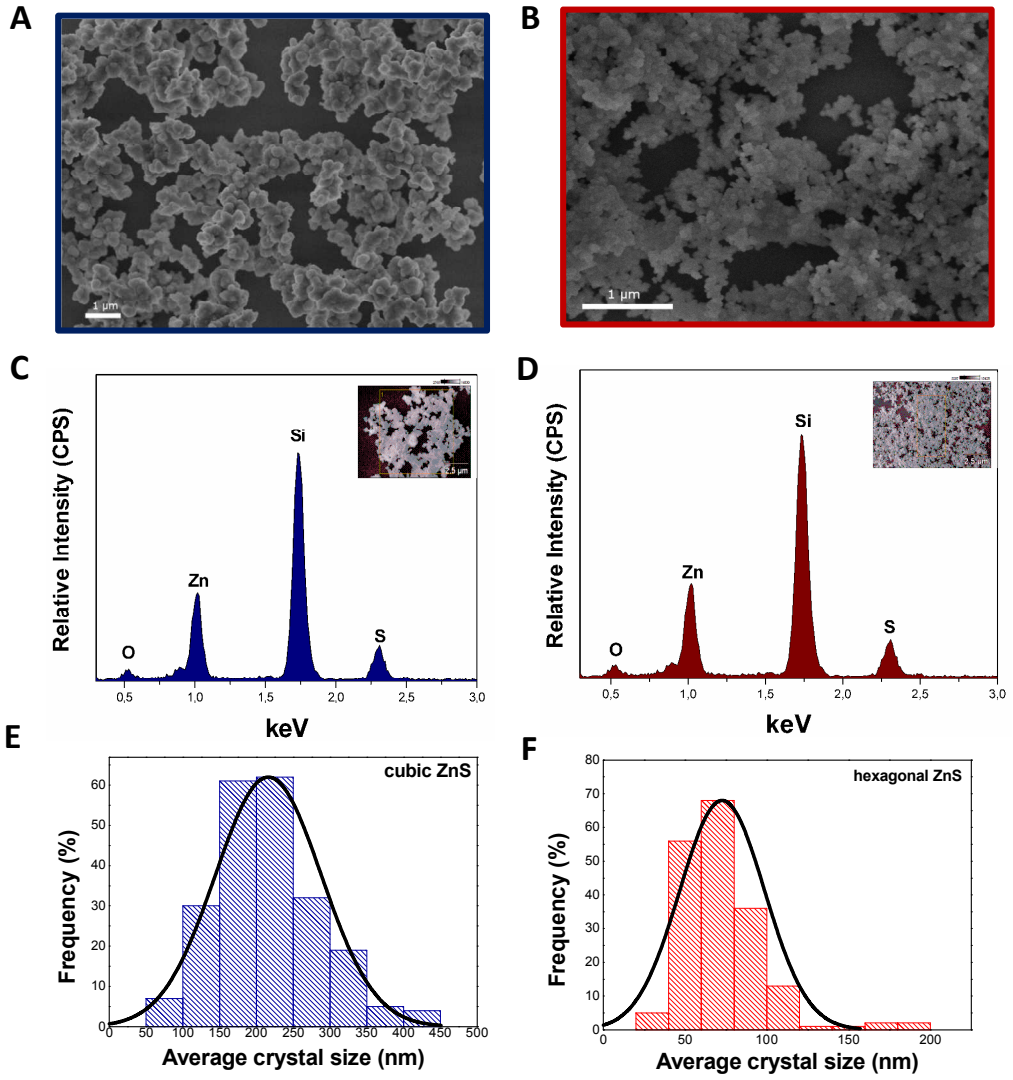
A
1 μm
B
1 μm
C
Relative Intensity (CPS)
O
Zn
Si
S
keV
D
Relative Intensity (CPS)
O
Zn
Si
S
keV
E
cubic ZnS
Frequency (%)
Average crystal size (nm)
F
hexagonal ZnS
Frequency (%)
Average crystal size (nm)

Figure 4.

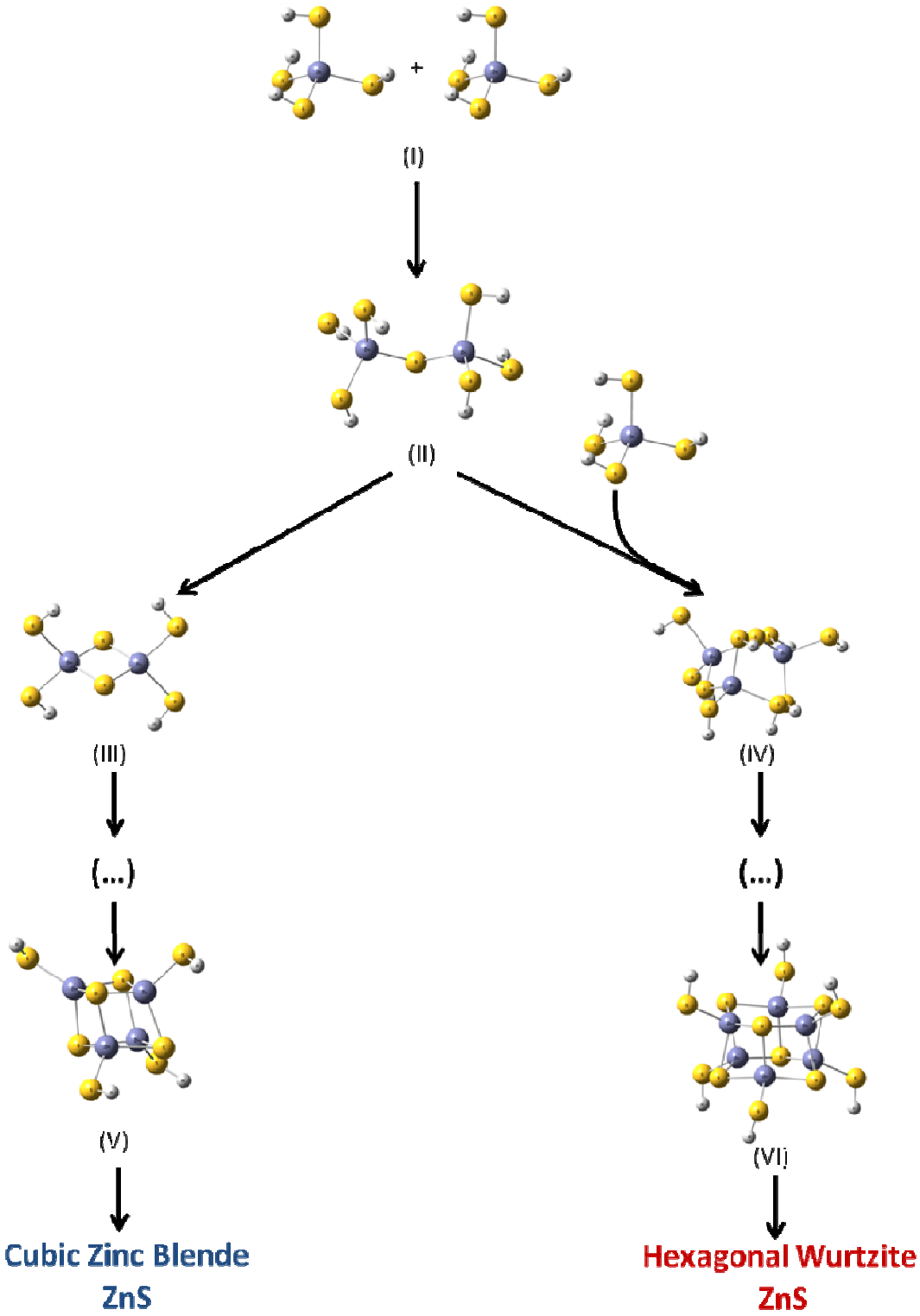

Figure 5.

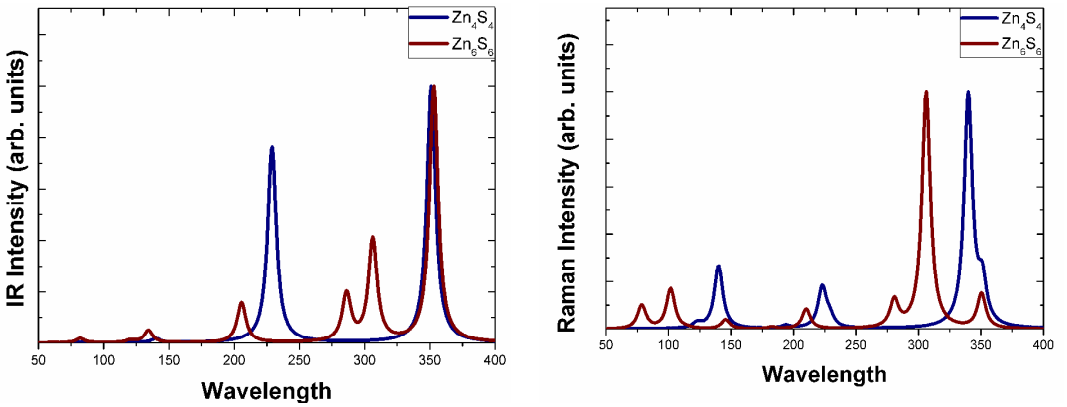
IR Intensity (arb. units)
Wavelength
50
100
150
200
250
300
350
400
Zn4S4
Zn5S6
Raman Intensity (arb. units)
Wavelength
50
100
150
200
250
300
350
400
Zn4S4
Zn5S6

(a) (b)

Figure 6.

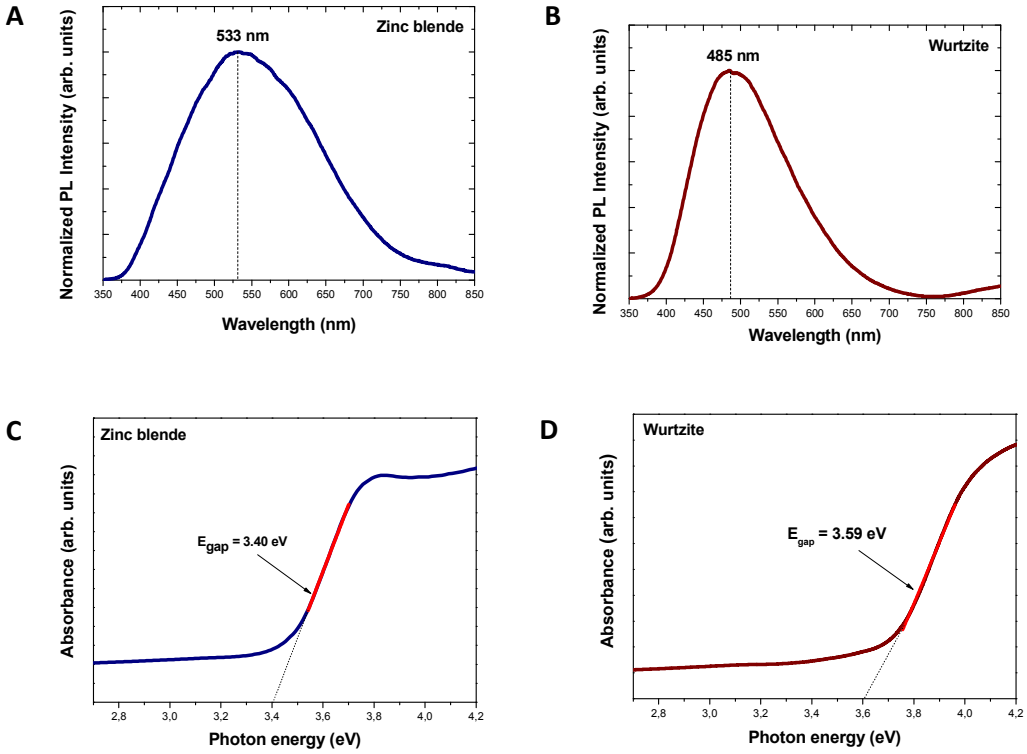
A
Zinc blende
533 nm
Normalized PL Intensity (arb. units)
Wavelength (nm)
B
Wurtzite
485 nm
Normalized PL Intensity (arb. units)
Wavelength (nm)
C
Zinc blende
E_gap = 3.40 eV
Absorbance (arb. units)
Photon energy (eV)
D
Wurtzite
E_gap = 3.59 eV
Absorbance (arb. units)
Photon energy (eV)

Figure 7.

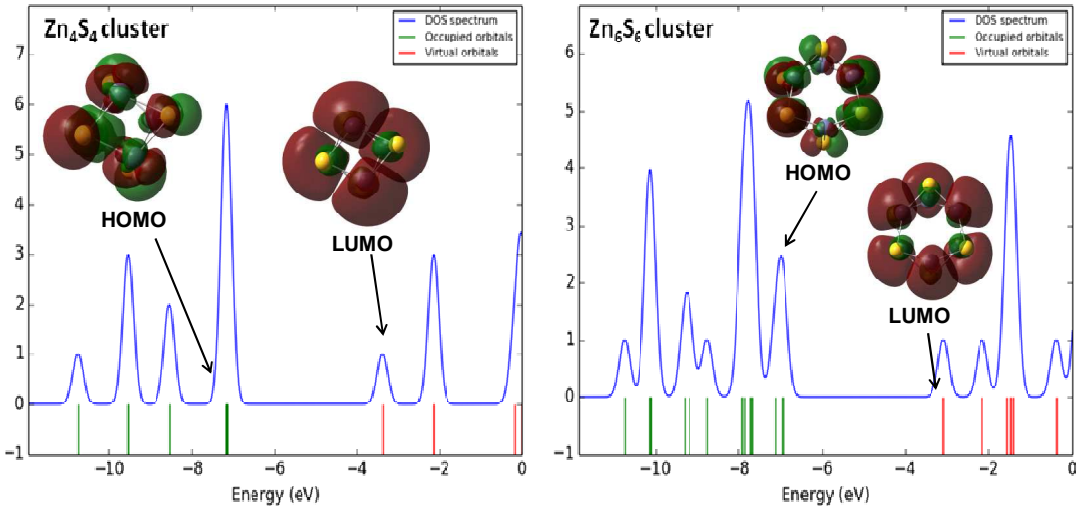
Zn4S4 cluster
DOS spectrum
Occupied orbitals
Virtual orbitals
HOMO
LUMO
Energy (eV)
Zn6S6 cluster
DOS spectrum
Occupied orbitals
Virtual orbitals
HOMO
LUMO
Energy (eV)

(a) **(b)**

Figure 8.

Structures	XRD particle size (Å)	Reaction yield (%)
W	20.20	91.59
ZB	17.72	67.88

Table 1.

Lattice parameter	ICSD*		MAS	
	Zinc Blende	Wurtzite	Zinc Blende	Wurtzite
***a* (Å)**	5.32	3.82	5.48	3.80
***c* (Å)**	-	6.26	-	6.24
R_{wp} **(%)**	-	-	10.88	6.23
R_p **(%)**	-	-	7.71	5.24
R_b **(%)**	-	-	0.561	0.303
X^2	-	-	0.897	2.679

* ICSD no. 41985 and 67453, respectively.[60]

Table 2.

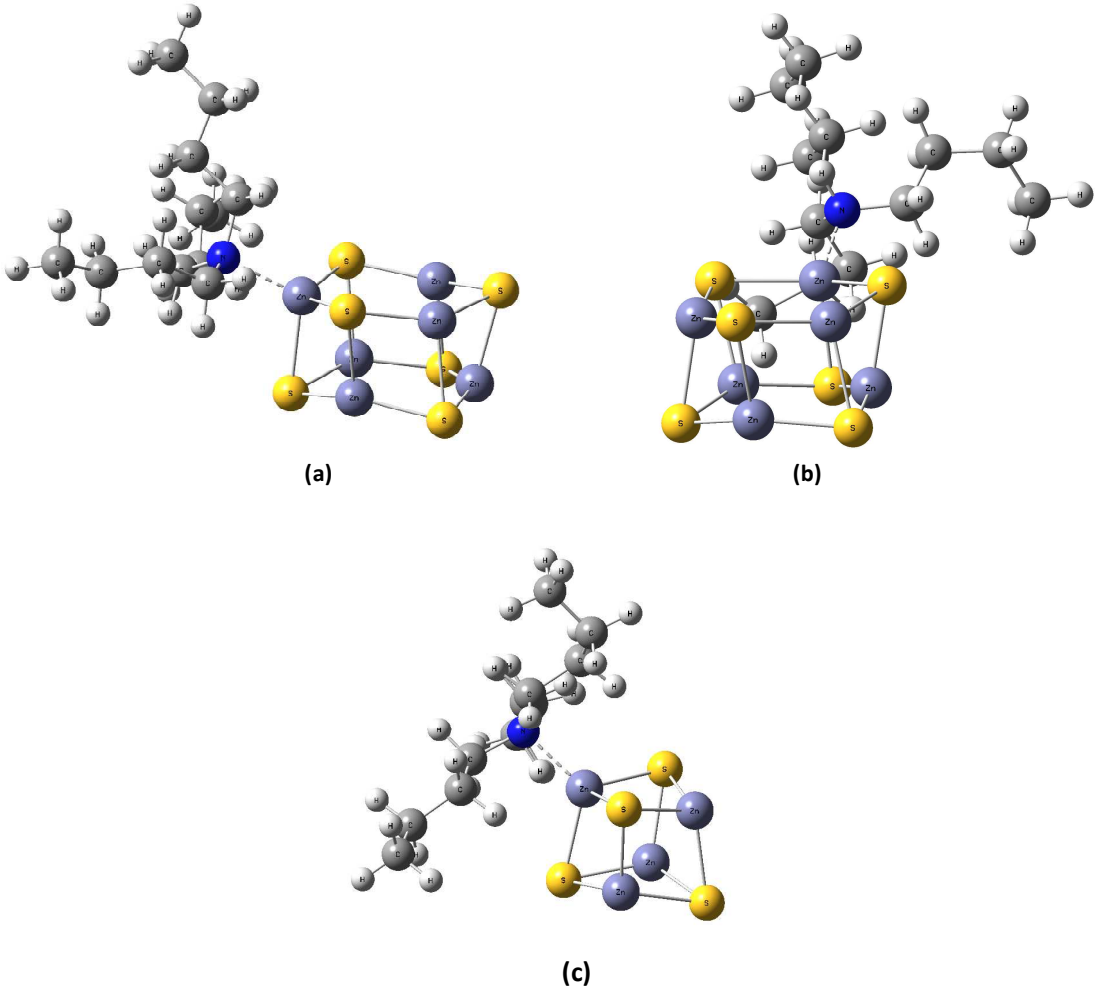

Model	Bond Length $_{Zn-N}$ (Å)	Angle [N-Zn-S] (°)	ΔE_{inter} (kcal.mol^{-1})
Zn_6S_6 Site A	2.18	114.03	-87.27
Zn_6S_6 Site B	2.15	110.47	-94.23
Zn_4S_4	2.10	117.04	-30.87

Table 3.

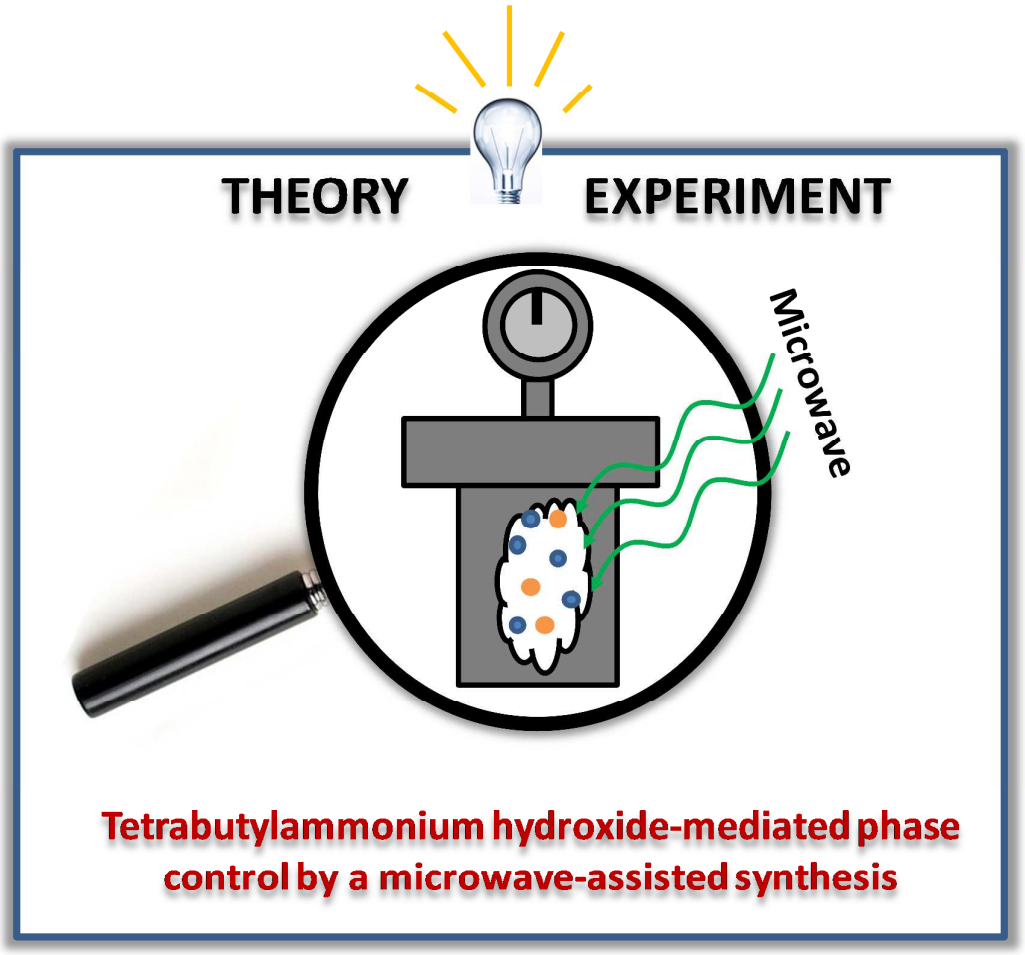

We demonstrated phase control, mediated by the presence of tetrabutylammonium hydroxide, in the growth of ZnS crystal that by using a low cost effectiven MAS method, a very moderate temperature (140 °C) and a very fast reaction time are sufficient to produce nanostructures with good degree of crystallinity.